

# **Journal of Thermal Engineering**

Web page info: https://jten.yildiz.edu.tr DOI: 10.14744/thermal.0000977



# **Research Article**

# Thermal performance optimization of wickless heat pipes using flash evaporation for distillation

Samah E. AL-SA'DI<sup>1</sup>, Dhamyaa S. KHUDHUR<sup>1,\*</sup>, Akram W. EZZAT<sup>2</sup>, Eric HU<sup>3</sup>

<sup>1</sup>Department of Mechanical Engineering, College of Engineering, Mustansiriyah University, Baghdad, 10052, Iraq <sup>2</sup>Department of Mechanical Engineering, College of Engineering, University of Baghdad, Baghdad, 10071, Iraq <sup>3</sup>Department of Mechanical Engineering, Faculty of Engineering, Computer and Mathematical Sciences, the University of Adelaide, 5005, Australia

# **ARTICLE INFO**

*Article history* Received: 21 May 2025 Revised: 27 May 2025 Accepted: 22 July 2025

# **Keywords:**

Flash Vaporization; Jet Nozzle; Saturation Temperature; Superheat; Thermosyphon; Wickless Heat Pipes

### **ABSTRACT**

This study presents a numerical and experimental investigation of the effect of flash evaporation on the thermal performance of a wickless heat pipe used in desalination applications. Moreover, this study examines the factors that affect flashing efficiency, such as the feed water mass flow rate, inlet temperature, and cooling water flow rate. High-temperature liquid in the range of 373K-393K becomes superheated when injected through a jet nozzle into a wickless heat pipe. This study focuses on using a jet nozzle type with a small diameter (0.4 mm). The steady value of the mass flow rate of the water is 0.00138 kg/s. Computational Fluid Dynamics (CFD) was used to simulate the two-phase flow and heat transfer processes in a heat pipe, which involves evaporation, condensation, and phase change. This study is unique in that it employs a non-homogeneous multiphase model to capture these processes. The results indicate that increasing the inlet temperature of liquid water leads to a rise in flashing vapor to a certain extent, thereby increasing the condensate flow rate. The maximum condensate flow rate was observed at 388K. The findings suggest that flashing efficiency improves as the condensate flow rate and inlet temperature increase. The optimum flash efficiency was found to be 80% at 393K. A strong agreement was observed between the experimental data, numerical temperature profiles, and the heat pipe's thermal performance.

Cite this article as: Al-Sa'di SE, Khudhur DS, Ezzat AW, Hu E. Thermal performance optimizationofwicklessheatpipesusingflashevaporationfordistillation.JTherEng2025;11(6):1601-1617.

### INTRODUCTION

Water is an essential resource for human survival, commonly sourced from lakes, reservoirs, and groundwater. Over the past decades, numerous methods and equipment have been developed to produce fresh water from these sources [1]. However, scientists and experts remained concerned about sewage pollution in rivers and lakes. Numerous devices and methods have been built in recent decades with the intention of creating fresh water [2]. Desalination technologies are used for various

Editor-in-Chief Ahmet Selim Dalkilic



<sup>\*</sup>Corresponding author.

<sup>\*</sup>E-mail address: damiaamech@uomustansiriyah.edu.iq This paper was recommended for publication in revised form by

purposes to extract fresh water from the limitless source of seawater; however, majority of these methods require a significant amount of energy [3]. Relevant and reliable heat dissipation technologies must be developed to advance distillation technologies and address these challenges; distillation devices must be designed to ensure safety, dependability, and system longevity [4,5]. Flash evaporation is one of the recent methods used in desalination [6]. When the surrounding pressure abruptly drops below the saturation pressure corresponding to the liquid temperature, flash evaporation occurs. Accordingly, the liquid becomes superheated. This notion means that the temperature of the liquid is higher than its saturation point, resulting in a highly thermodynamic unstable condition known as liquid superheat. Thereafter, sensible heat is rapidly converted into latent heat as the liquid vaporizes to reach a new thermodynamic equilibrium state [7]. This study utilizes a wickless heat pipe for flash evaporation desalination. Heat pipes have long been recognized as efficient devices for transferring heat from a source to a sink. Moreover, heat pipes have been widely used in various applications, such as solar energy harvesting, waste heat recovery, space vehicles, and in cooling electronic and electrical components [8]. A heat pipe is a sealed, narrow tube with closed ends. After the pipe is evacuated, it is filled with a specific amount of liquid. One end of the pipe is connected to a heat sink, while the other end is exposed to a heat source. The condenser is the sink end, and the evaporator is the source end. These two ends are separated by the intermediate section of the pipe, known as the adiabatic area. The fluid in the heat pipe absorbs heat as it vaporizes in the evaporator and releases it as it condenses in the condenser [9]. The wick-form lining of traditional heat pipes helps return the condensate to the evaporator through the capillary effect. Wickless heat pipes, which rely solely on gravity instead of capillarity, will be introduced later. The orientation is constrained by positioning the condenser above the evaporator. Wickless heat pipes are also referred to as thermosiphons [10]. The thermal performance of heat pipes is primarily determined by their working fluids. Given that water has the highest latent heat and a good boiling temperature, it is widely recommended for various applications; however, other fluids should also be carefully evaluated [11,12].

Several researchers have investigated different designs and applications of wickless heat pipes. Mameli et al. [13] found that the utilization of multiple heaters in a closed-loop thermosyphon enhances its performance. Their experiments with different heater placements demonstrated that asymmetrical arrangements improved fluid circulation and ensured stable operation. The thermosyphon using FC-72 as the working fluid exhibited more efficient heat dissipation than traditional methods, indicating its potential for electronic cooling and thermal management. Alamnar et al. [14] developed a new CFD model to examine how varying tilt angles (10°, 30°, 50°,

70°, and 90°) and fill ratios (25%, 35%, 65%, 80%, and 100%) affect thermosiphon performance. ANSYS Fluent was used to conduct a CFD simulation of two-phase flow inside a thermosiphon heat pipe (THPs) to investigate the temperature distribution and the effect of thermal resistance on thermal performance. The CFD results showed that the evaporator temperature increased for low tilt angles and low fill rates. The lowest heat resistance was observed at a fill ratio of 65% and a tilt angle of 90°. Comparison with experimental results showed remarkable consistency, with maximum variances for thermal resistance and temperature distribution of 8.1% and 4.2%, respectively. Marc et al. [15] numerically and experimentally examined a counter-current two-phase thermosyphon with cascading pools. The pools were utilized to cascade the working fluid to the evaporator end cap. They predicted and validated the experimental outcomes of the novel design using a numerical model and a control volume technique. The results showed that the thermosyphon stages were suitable for the study and for evaluating the effect of design changes. Naresh et al. [16] conducted an experimental study on heat transmission in thermosiphons using six fins with a regular cross-sectional area across the condenser portion. This study utilized three fill rates (20%, 50%, and 80%) and power levels ranging from 50 W to 275 W, with water and acetone as the charging media. The test results showed that the use of these fins enhanced condensation and improved the thermal performance of the device by 17% in terms of sink and source temperature reduction and 35.48% in terms of thermal conductivities at low heat inputs. Naruka et al. [17] conducted an experimental investigation using three distinct working fluids (water, methanol, and acetone) to estimate the thermal performance of THPs. The experiment used four different tilt angles (0°, 30°, 45°, and 60°) and four input heat levels (10, 15, 20, and 25 W). The results showed that the THP with acetone achieved 31.8% higher efficiency compared with water, with the optimal tilt angle for thermal efficiency being 45°. Heat pipes charged with methanol and acetone efficiently performed in this application, with minimal heat dissipation.

Gorecki et al. [18] in this paper, a finned heat pipe heat exchanger utilized as a recuperator in small air conditioning systems with airflow rates of 300–500 m³/h is modeled, designed, and experimentally validated. R404A was found to be the ideal working fluid at a 20% filling ratio after a thermal model was created utilizing known correlations. A staggered configuration of 20 finned heat pipe rows was suggested by parametric analysis utilizing the model, which produced a steady efficacy of about 60%. While maintaining a pressure drop below 150 Pa, additional optimization through the use of a brute-force technique increased effectiveness to 66%. With a relative error of less than 10%, the experimental data closely matched the predictions of the model.

Alaa et al. [19] studied the thermal performance of a thermosyphon heat pipe (THP) influenced by a novel tube packing (TP). The THP pipe measured 600 mm in length with an inner diameter of 17.4 mm and was made of copper. The experimental results demonstrated that the TP-THP exhibited significantly enhanced heat transfer efficiency, reducing transit time by 31% and thermal resistance by 17%-62%. Samah et al. [20] compared two types of wickless heat pipes: loop type (LT) and straight type (ST). Both systems featured identical evaporator and condenser geometries. The evaporator consisted of a rectangular box with a heating element, and the condenser was a vertical tube cooled by a water jacket. The test was performed with 10 input powers and four fill ratios. The results showed that the LT was more efficient than the ST, exhibiting lower wall temperatures and thermal resistance. The 50% fill ratio consistently resulted in the lowest wall temperatures across all input powers. Hohne [21] conducted a numerical analysis of the thermal performance of a heat pipe using computational fluid dynamics (CFD) to continuously model the two-phase flow of steam and water and heat transfer. The study's uniqueness lies in the use of a homogeneous multiphase model to represent the evaporation, condensation, and phase change processes and the implementation of source terms influenced by the Lee phase change model. In this study, the evaporation and condensation processes inside a heat pipe were validated and compared with earlier research findings from the literature. The evaluation of the heat-pipe's thermal performance and the comparison of the CFD temperature profiles with experimental data indicated a reasonable level of agreement. The heating power should not exceed 1000 W for the type of heat pipe design studied, which was constructed using copper. Ayad and Qusay [22] conducted a numerical education on the thermal performance of a wickless heat pipe (thermosyphon) using 2D CFD with ANSYS Fluent. They studied the supply of temperature and the thermal resistance along the thermosyphon under different working circumstances, considering tilt angle, fill rate, and heat input as key parameters. The results indicated that the influence of filling ratios on the mean wall temperature of the evaporator is greater at high heat inputs than at low heat addition. Ali et al. [23] experimentally examined the thermal performance of heat pipes by observing the influence of the wick and working fluids in a vertical orientation. Water, methanol, ethanol, and various binary combinations with mixing ratios of 50%, 30%, and 70% were used as the working fluids. The findings indicated that the thermal resistance of heat pipes charged with pure and binary mixtures of working fluids reduced with increasing heat inputs. In recent years, several studies have focused on enhancing flash evaporation processes. Wang et al. [24] The performance of a thermosiphon heat pipe with two evaporating surfaces, one corrugated and the other smooth, was studied. The results showed that the corrugated pipe achieved better thermal performance, recording the lowest total thermal resistance of 0.0243

K/W. Numerical simulations (CFD) also showed that the corrugations in the pipe promote fluid boiling within the grooves, improving heat transfer efficiency in the region above the fluid level. Compared to conventional pipes, the corrugated design also offers higher stability and reliability.

The thermal performance of a wickless heat pipe used for electronic cooling with a flat evaporator (100×100×30 mm) is investigated numerically by Samah et al. [25]. EES software was used to assess various fill ratios (15%, 25%, 50%, 85%), input powers (10–100 W), and cooling water flow rates (0.0083–0.033 kg/s). With minimum evaporator and condenser thermal resistances of 0.07°C/W and 0.14°C/W, respectively, the results indicated that the best performance happened at a 50% fill ratio. 0.016 kg/s was the ideal water flow rate.

El-Fiqi et al. [26] conducted an experimental study on the flash vaporization of superheated liquid jets. The study used tap water at low pressures and investigated the effects of superheat degree, inlet temperature, and feed flow rate on flash vaporization. The amount of flashed vapor was determined through condensation measurements and compared with the calculated values. The relationship between superheat degree and flashed vapor was evaluated. The flashing efficiency was measured and compared with previous results. Akram and Radwan [27] developed an experimental setup to investigate the flash evaporation of upward water flow in a 1.8 m vertical pipe. The authors investigated the effects of hydrogen bubble injection and water electrolysis on the flash evaporation process. The findings indicated that both methods increased steam quality and reduced non-equilibrium temperature differences. The experimental results were compared with the theoretical predictions based on a two-phase flow model. Lapka et al. [28] investigated the effect of nozzle shape on flash boiling. The mixture model was used to simulate two-phase flow, and the Zwart-Gerber-Belamri model was utilized for phase change. Simulations were conducted for different nozzle diameters (0.62, 0.72, and 0.82 mm), pressures (5-7 bar), and undercoolings (1-50 K). The results indicated that the nozzle shape had no influence on the mass flow rate of flashing water. Fathinia et al. [29] investigated a low-temperature thermal desalination flash evaporation system. The researchers found that the undefined temperature follows an exponential decay curve, aligning well with the temperature distributions observed in various flash evaporation scenarios. Moreover, increasing the spray flow rate results in high flash evaporation, while decreasing the jet flow rate enhances evaporation. John et al. [30] presented a novel model for flash evaporation, a challenging process due to its high-pressure and high-temperature conditions. The model, developed using Open FOAM, utilizes a dual-diameter approach and a critical nucleation-based mass transfer limit. This model demonstrates excellent agreement with the experimental data for area-averaged pressure and volume fractions. Inter-momentum forces are crucial for accurate momentum transfer prediction in

bubble-dominant flows. Although radial volume fraction predictions show room for improvement, sensitivity studies reveal the model's responsiveness to parameter changes. Cai et al. [31] carried out an experimental investigation to examine the thermal behavior of spray flash evaporation at high pressures and temperatures, emphasizing the impact of superheat level and liquid mass flow rate on vapor production. Similarly, Ji et al. [32] conducted a numerical study on the internal flow properties of a nozzle with S-shaped vanes, demonstrating the effects of geometric changes on the flow distribution and flashing process. Furthermore, a droplet-based model was used in a different work by Cai et al. [33] to describe the dynamics of flash evaporation and evaluate how droplet size and inlet temperature affect flash efficiency. The present study, which uses a wickless heat pipe and a fine-diameter jet nozzle, is based on these recent contributions, which highlight the significance of nozzle shape, fluid conditions, and modeling approaches in comprehending and optimizing flash evaporation.

Despite numerous studies on wickless heat pipe modeling and flash evaporation in distillation, the novelty of this study lies in its integrated numerical and experimental investigation of flash boiling within a wickless heat pipe using a micro-scale jet nozzle. This study aims to utilize a non-homogeneous multiphase model of a wickless heat pipe with flash evaporation induced by a 0.4 mm microscale jet nozzle to simulate evaporation, condensation, and phase change phenomena. This setup enables high-intensity evaporation under elevated pressures and temperatures, which has not been comprehensively explored in prior literature. Unlike conventional approaches, this study utilizes a validated 3D non-homogeneous multiphase CFD model to simulate phase-change behavior and compares these results with experimental data. This study highlights how inlet temperature, cooling flow rate, and feed flow rate influence flashing efficiency. This advancement marks a measurable enhancement over prior work and supports the system's potential for scalable, high-performance thermal desalination applications.

# **NUMERICAL METHODOLOGY**

### **Physical Model**

Pressurized water is heated at the supply water tank by an electrical heater, and then the hot water flows through the jet nozzle. After the hot water passes into the jet nozzle, an expansion of the flow occurs as a result of the internal energy being converted into kinetic energy. A sudden change in pressure occurs, and the temperature decreases as a result of flash evaporation in the throat nozzle area, and thus the flow speed increases. The amount of liquid converted to vapor flow passed through the heat pipe; the liquid-vapor mixture reached the condenser section, where the vapor formed was re-condensed to liquid for reuse. Various flow parameters, including outlet nozzle

temperature, saturation temperature and pressure, velocity, thermal resistance, flash efficiency, heat transfer coefficient, and evaporation rate, were measured. Excellent comparisons are provided by the experimental data to validate the recently created methodology. The liquid-vapor mixture in the condensing portion was cooled by cold water, which considerably lowers its temperature when compared to the input. The mass transfer rate downstream of the throat appears to have been impacted by this. In this work, the temperature of water entering the test section is increased in order to increase the flash evaporation in the system.

### **Computational Model**

The thermal performance of a wickless heat pipe with flash evaporation induced by a jet nozzle is investigated through 3D numerical simulations with ANSYS Fluent 22.2. Water is used as the working fluid, circulating within a cooper double-pipe heat pipe. A numerical simulation of the computational domain in (Fig. 1). The two-phase flow is simulated using the volume of fluid (VOF) approach, which accurately tracks the vapor–liquid boundary. The following presumptions are used:

- 1. The layered annular topology of the flow domain allows for axisymmetric modeling.
- The flow field is considered transient and three dimensions.
- 3. Liquid condensate is regarded as the secondary phase, while water vapor is treated as the primary phase.
- Although thermal energy exchange incorporates flash evaporation effects, the two-phase flow is regarded as incompressible.
- Non-slip boundary conditions are used at the heat pipe wall.
- 6. Surface tension and wall roughness are disregarded.
- 7. Heat conduction governs the copper wall, which is regarded as a solid domain.
- The inlet boundary is defined as a pressure-inlet and the exit as a pressure-outlet to allow flashing to naturally develop.
- Symmetry: A symmetry plane is utilized along the model's longitudinal axis, based on the system's geometric and thermal symmetry, to save computational costs.

### **Governing Equations**

The governing equations for the computational domain must be solved to conduct a numerical simulation of the thermal performance of the heat pipe. In this study, the VOF assumption is applied to the fluid and solid domains. The 3D governing fluid flow, heat/mass transfer, momentum, and energy equations of this study are used for the solid and fluid domains, according to previous assumptions. The solid domain (copper pipe) is governed by the energy equation. Meanwhile, the water-vapor flow is governed by continuity, momentum, and energy equations. The examined situation is solved using these equations to determine the transient and steady-state velocities and temperatures [34]:

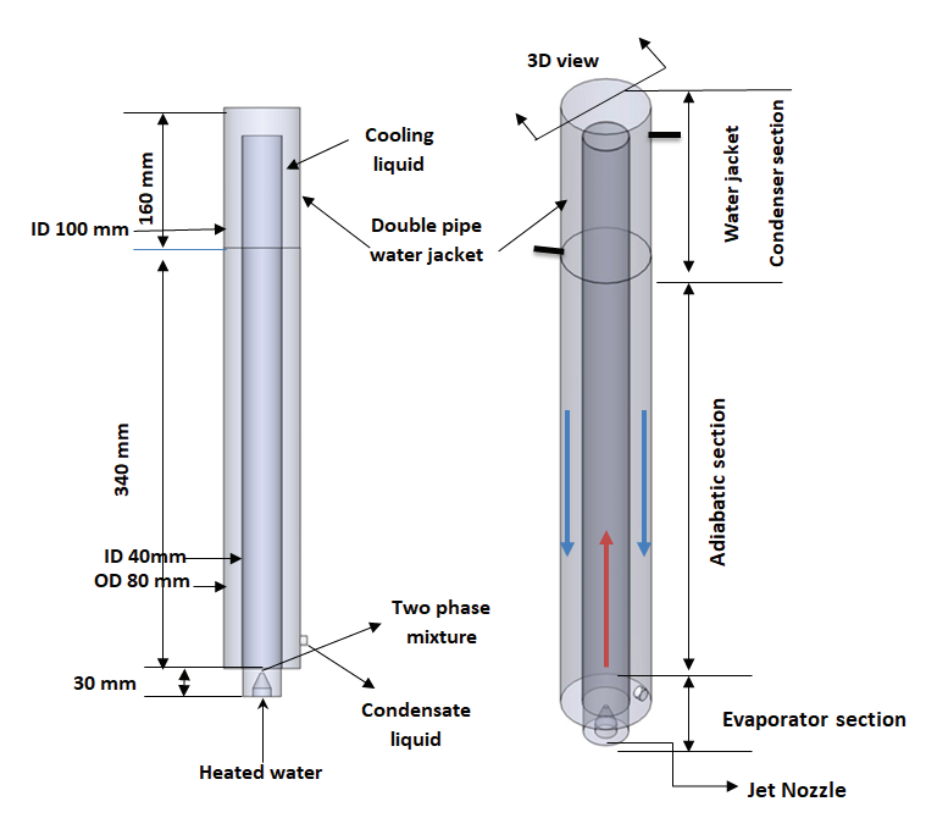


Figure 1. Straight heat pipe (SHP) model geometry and dimensions.

**Continuity Equation** 

$$\nabla \cdot (\alpha_l \, \rho_l v) = -\frac{\partial}{\partial t} (\alpha_l \, \rho_l) + S_m \tag{1}$$

$$\rho = \propto_l \rho_l + (1 - \propto_l) \rho_v \tag{2}$$

Momentum Equation

$$F_{CSF} = 2\sigma \frac{\alpha_l \rho_l C_v \nabla \alpha_v + \alpha_v \rho_v C_l \nabla \alpha_l}{\rho_l + \rho_v} \tag{3}$$

The following momentum equation is utilized in the VOF model to account for the influence of  $F_{CSF}$  forces:

$$\frac{\partial}{\partial t}(\rho \vec{V}) + \nabla \cdot (\rho \vec{V} \vec{V}) = \vec{g} - \nabla p + \nabla \cdot [\mu(\nabla \cdot \vec{V} + (\nabla \cdot \vec{V}^T))] + \overrightarrow{F_{CSF}}$$

$$(4)$$

The dynamic viscosity  $\mu$  is computed as follows, taking into account a mass average:

$$\mu = \propto_I \mu_I + (1 - \propto_I) \mu_{II} \tag{5}$$

**Energy Equation** 

The energy equation is presented as follows:

$$\frac{\partial}{\partial t} (\rho E) + \nabla (\overrightarrow{V} \rho E) = \nabla \cdot (k \nabla T) + \nabla \cdot (pV) + S_E$$
 (6)

Energy source parameter  $S_E$  is added to calculate the heat transfer during the condensation and evaporation processes.

$$E = \frac{\alpha_l \rho_l E_l + \alpha_v \rho_v E_v}{\alpha_l \rho_l + \alpha_v \rho_v} \tag{7}$$

$$E = C_{v,l}(T - T_{sat}) \tag{8}$$

$$E = C_{v,v}(T - T_{sat}) \tag{9}$$

# **Boundary Conditions**

Boundary conditions are defined in the current numerical simulation to accurately depict the flash evaporation and condensation processes inside the wickless heat pipe and closely mimic the experimental configuration.

Inlet: The gauge pressure and saturation temperature of the incoming liquid water are defined using a pressure-inlet boundary condition. The incoming fluid is assumed to be entirely in the liquid phase (zero vapor volume fraction). The inlet pressure is adjusted between 1 bar and 2.5 bars to examine its influence on flashing behavior. This configuration enables the simulation to accurately depict the beginning of flashing due to pressure loss inside the nozzle instead of imposing a set mass flow rate.

<b>Table 1.</b> The boundar	y conditions used	l in t	he CFD	simulation
-----------------------------	-------------------	--------	--------	------------

Name	Description
Constant inlet temperature	373, 378, 383, 388, and 393 K
Constant inlet water cooling system temperature	293, 293.5, 300, 300.5, and 300 K
Constant heat transfer coefficient of the condenser	4937, 4582, 4355, 4076, and 3874 W/m <sup>2</sup> .k

- Outlet: A pressure-outlet boundary condition is assigned at the condenser exit, assuming ambient atmospheric pressure. This condition enables free outflow of vapor and liquid without artificially constraining the phase composition.
- Walls: Convective heat transfer conditions are imposed on the condenser section walls, with a heat transfer coefficient derived from the experimental cooling water flow data. In all adiabatic sections of the pipe, no heatflux (adiabatic) boundary conditions are observed.

The chosen boundary conditions reflect realistic experimental parameters, including inlet water temperature, pressure, and average cooling water temperature. A summary of all applied boundary conditions and their values is presented in Table 1.

# Mesh Independence

The computational grids for the wickless heat pipe simulations with a jet nozzle are generated using tetrahedral elements via ANSYS Meshing (Fig. 2). This approach facilitates high-quality mesh generation for complex 3D geometries and significantly reduces computational cost. Global and local sizing functions are applied to control mesh density near walls and regions of interest. Mesh quality is evaluated based on orthogonal quality, aspect ratio, and skewness, in accordance with Fluent meshing best practices [34-36]. The orthogonal quality scale ranges from zero to one, with zero denoting a mesh of low quality. A minimum orthogonal quality of  $\geq 0.01$  must be maintained. The aspect ratio's value is important for wall functions and must be sufficiently low to accurately capture flow behavior near the walls. Lastly, the skewness rate, which is inversely related to the solution accuracy, must be kept as low as possible to minimize numerical error [37]. The orthogonal quality of the meshes used in this study is 0.924, with a minimal value of 0.39. The aspect ratio is 7.596, and the skewness rate is 0.19. These values confirm compliance with the recommended criteria for high mesh fidelity. Inflation layers are implemented along the wall surfaces to accurately capture near-wall behavior in the evaporator and condenser zones. Moreover, the y<sup>+</sup> parameter is monitored throughout the domain and remained below five near all critical heat transfer surfaces, ensuring that the mesh resolution is sufficient to resolve boundary layer effects without the need for wall functions. A mesh independence study is conducted using five mesh densities: 586,600, 1,386,654, 2,619,052, 3,708,894, and 5,488,044 cells. The simulation results showed convergence beyond 2.6 million elements. The average temperature variation in the cooling water jackets between 2.6 million and 3.7 million grids is less than 0.16, confirming mesh independence (Fig. 3).

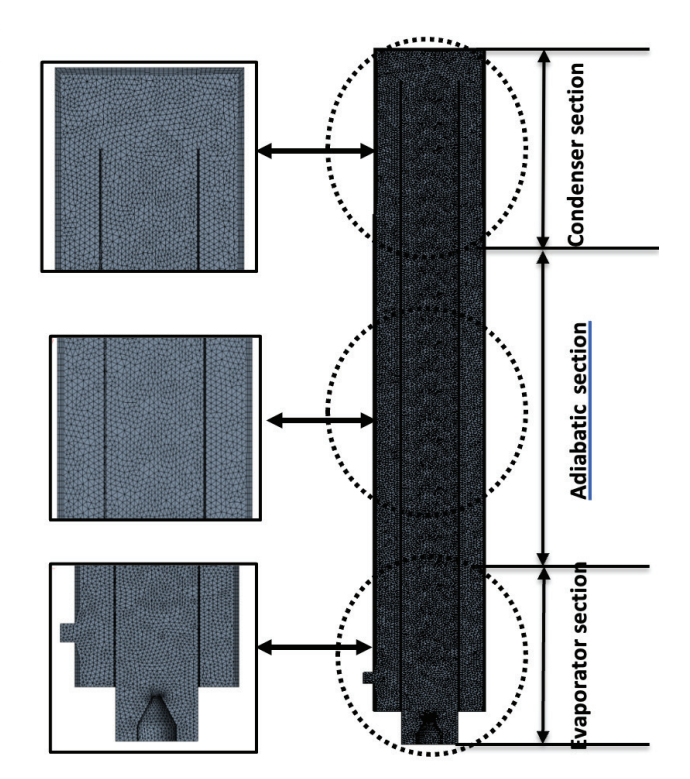
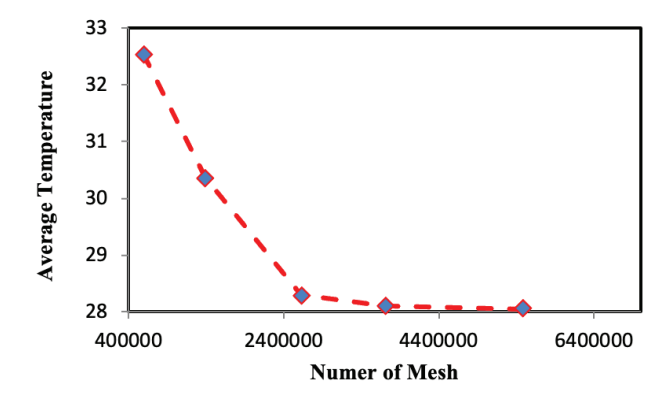


Figure 2. Mesh of the SHP.



**Figure 3.** Mesh independence with a cooling water jacket

#### **Numerical Solution**

The numerical simulation is carried out using the ANSYS Fluent 22.1 solver and a pressure-based, transient formulation to represent the unsteady behavior of the twophase flow and heat transfer process. The governing equations are discretized using second-order upwind schemes for convective terms and central differencing for diffusive terms. The interface between the liquid and vapor phases is tracked using the VOF model with a compressive interface capturing scheme. The simulation used an adaptive time-stepping approach, and the results are monitored until a quasi-steady state is reached. The convergence criteria are set to 10<sup>-3</sup> for the continuity, momentum, and volume fraction equations and 10<sup>-6</sup> for the energy equation. The simulations are continued until t = 90 s, by which point all residuals had met their convergence thresholds for all cases considered.

# **EXPERIMENTAL SETUP**

The experimental apparatus used in this study is illustrated in Figure 4. This apparatus consists of five main components: the test section (a wickless heat pipe with an integrated jet nozzle), a supply water tank, a condensate collection tank, connecting pipes, and measurement

instruments. All fittings and joints are thoroughly sealed and tested to ensure leak-free operation and accurate data acquisition. The test section consists of a double-pipe made of acrylic (thermal conductivity  $k = 0.18 \text{ W/m} \cdot \text{K}$ ) [38], with the evaporator positioned at the lower section and the condenser at the upper end to facilitate gravitational return of the condensate. Flash evaporation occurs at the nozzle outlet due to a sudden pressure drop. The generated vapor flows through an acrylic pipe (inner diameter: 36 mm, outer diameter: 40 mm, and length: 500 mm) to the condenser, where it is cooled by a surrounding water jacket (length: 200 mm, inner diameter: 96 mm, and outer diameter: 100 mm). Thereafter, the condensate returns to the collection tank via a return pipe (ID: 76 mm, OD: 80 mm, and length: 500 mm) located below the second pipe. All components are insulated with a glass wool to minimize heat losses. The jet nozzle, positioned at the entrance of the evaporator, is made of aluminum and has a 0.4 mm inlet diameter, 12.5 mm outlet diameter, and 30 mm length (Fig. 5). The chosen 0.4 mm nozzle size ensures controlled flash evaporation and is selected to match the operating pressure range of the system. The working temperature range (373– 393 K) is selected to replicate low-grade heat conditions typically available in practical desalination setups. The supply tank (300 mm diameter, 350 mm height, and 3 mm



**Figure 4.** Complete experimental testing device: (1) Heat pipe (2) Nozzle (3) Condenser (4) Water jacket (5) Connecting pipe (6) Water tank (7) Control panel (8) Electrical heater (9) Digital pressure valve (10) Pressure valve (11) Pressure safety valve (12) Control valve (13) Data logger (14) Charging storage (15) Clamp meter (16) Condensate storage.

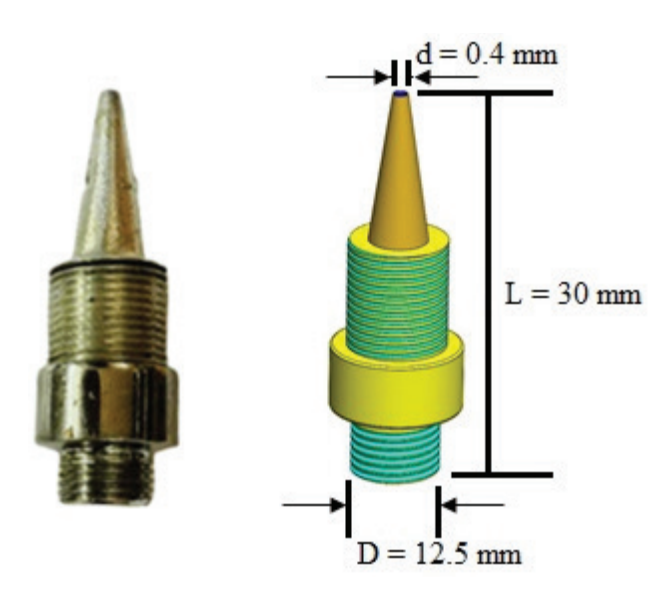
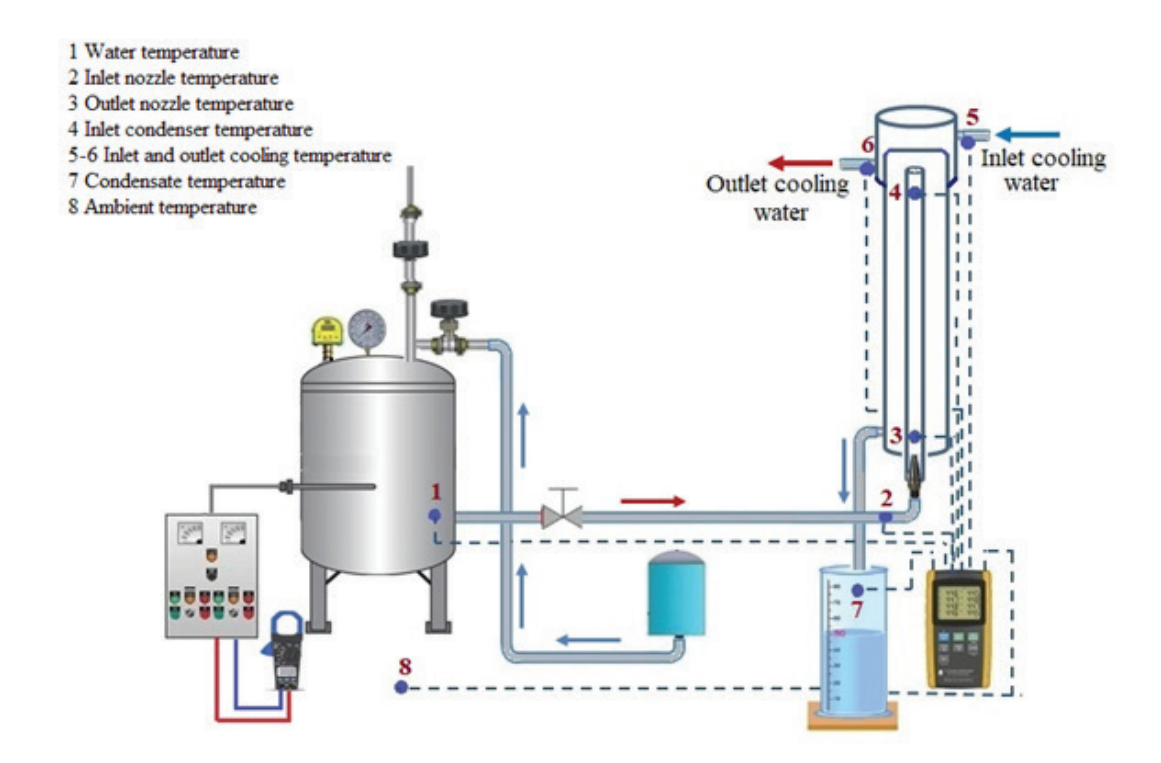


Figure 5. Jet nozzle diagram.

wall thickness) is fabricated from 6061 aluminum alloy. The tank can hold up to 14 kg of water and safely operate at pressures up to 10 bar. Moreover, the tank is equipped with a 4 kW electrical heater (adjustable between 0 W and 4000 W), powered by a 220 V AC source. Pressure regulation and thermal safety are ensured by a brass pressure relief valve, a thermostat-controlled contactor, and a pressure switch that disconnects the power supply when the pressure exceeds a predefined limit. A 220 V AC power source

supplies electricity to the heater. The heater's power supply can be adjusted between 0 W and 4000 W. The electrical heater is made of aluminum alloy, measures 200 mm long, and has a 4 kW capacity. The heater is securely attached to the left side of the water tank and powered by an input supply. Three control valves (6.25 mm diameter) manage fluid flow: one for filling distilled water, one for air discharge, and one for controlling flow to the test section. An additional valve is placed at the tank bottom for drainage. The water flow from the tank to the test section is directed through a copper pipe (12.5 mm diameter and 500 mm length) equipped with a flow-regulating valve. Pressure measurements are conducted using an analog pressure gauge and a digital pressure controller. The gauge, mounted on the tank, provides reference system pressure. Meanwhile, the digital controller—linked to a contactor—monitors and regulates system pressure by activating a cutoff mechanism in case of excessive pressure. The average value from both readings is used in the data analysis.

A temperature thermostat is used to measure the temperature of the fluid in the tank and is connected with a contactor to control the heater. If the temperature exceeds a predetermined limit, then the contactor is activated to shut off the heater, preventing overheating. A clamp meter is used to measure current and voltage. Thereafter, the power is computed by multiplying the voltage by the current. K-type thermocouples that had been calibrated (absolute inaccuracy of  $\pm 1^{\circ}$ C) are used for all temperature readings. Eight data points for temperature measurements



**Figure 6.** Schematic of the experimental test.

are carefully selected (Fig. 6). Thermocouples (no. 1) are connected to determine the liquid's temperature in the water tank. The temperature of the liquid inside the evaporator with the nozzle is measured by the thermocouple (no. 2). The evaporator output temperature is measured by one K-type (no. 3) thermocouple. The temperature of the vapor inside the condenser is measured by the thermocouple (no. 4). The fiberglass-insulated wires of the thermocouples are visible only at the junction area. The temperature of the cooling water jacket's input and output is measured by two thermocouples (nos. 5-6). Meanwhile, the condensate temperature is measured by the thermocouple (no. 7). The ambient temperature is measured using the thermocouple (no. 8). The heat pipe's temperature is tracked and recorded using a data logger. The data logger type (BTM-4208SD), which contains 12 channels, is compatible with various types of thermocouples (K, J, T, E, R, and S). The thermocouples are connected to the data logger through a special module. The system's internal pressure is examined using two pressure devices: a pressure gauge and a digital pressure control. The pressure gauge is placed on the boiler and is used to measure the system's initial pressure and verify the digital pressure readings. The second device is a digital pressure control that uses a digital pump switch to measure and automatically control system pressure, ensuring that the switch is disconnected via an electrical contractor when the pressure exceeds the specified limit. The average value of two readings is used.

# **TESTING PROCEDURE**

The experimental procedure is initiated by filling the water tank with distilled water via a liquid-level column located on the upper right side of the tank. The corresponding valve is opened to allow water to enter the evacuated tank, and the process is repeated as necessary until the desired water level is reached, as indicated on the level gauge. Once the tank is filled, all valves are closed, and the system is inspected to ensure that no pressure fluctuations or air leakage occurred. After the charging process, the heater is activated by switching on the control panel and engaging the voltage stabilizer. The heating power is gradually increased to the required level using a manual control system. The internal water temperature is regulated using

a thermostat connected to a contactor, which disconnects the power supply once the set point is reached. Once the water reaches the target temperature (within the range of 373-393 K), the control valve between the water tank and the test section is opened, allowing hot, pressurized water to flow into the heat pipe and pass through the jet nozzle. Flash evaporation occurred due to the sudden pressure drop at the nozzle, generating steam that is directed toward the condenser. Furthermore, the cooling water is circulated through the condenser jacket, and the inlet temperature of the cooling water is recorded. As the steam condensed within the condenser, the resulting liquid is collected in a calibrated condensate tank for mass flow rate measurement. Data acquisition is initiated at this point, with temperature readings monitored through the connected data logger. The system is allowed to run for 15-30 min until a steady-state condition is achieved, as indicated by stable temperature and pressure readings. Once steady-state is established, experimental measurements are continuously recorded for three hours. All temperature sensors are calibrated K-type thermocouples (±1°C accuracy) to ensure data accuracy, while the power input is measured with a clamp meter. Uncertainty in temperature and pressure readings is considered in the overall data analysis to enhance the reliability of the results.

# **UNCERTAINTY ANALYSIS**

Uncertainty analysis was performed for all important measurements and derived values to guarantee the accuracy of the experimental and numerical results. The estimated uncertainties of the instruments used in the experiment are summarized in the table 2. The uncertainty in derived values including heat input, heat rejected, thermal resistance, and flash efficiency was calculated using error propagation.

The estimated uncertainties in computed quantities, based on uncertainty propagation, are:

- Heat rejected (Qcond): ±3.5 %
- Thermal resistance (Rcond): ±4.0 %
- Flash efficiency (ηflash): ±4.2 %
- CFD prediction (numerical): ±2.0 %

These degrees of uncertainty validate the accuracy of the simulation and measurements and fall within reasonable engineering bounds.

**Table 2.** The uncertainty of parameters

Measured Quantity	Instrument / Method	Uncertainty	
Temperature (water, vapor)	K-type Thermocouple	±1°C	
Flow rate (cooling water)	Rotameter	±1%	
Condensate mass	Digital Balance	±0.001 kg	
System Pressure	Bourdon gauge + Digital Controller	±0.5%	
Voltage & Current	Clamp Meter	±2%	

### **EVALUATION PARAMETER**

The performance of the flash evaporation system is evaluated based on several key thermal and flow parameters derived from experimental measurements:

- Inlet Temperature (T<sub>in</sub>) is determined as the average temperature recorded by thermocouples positioned along the central section of the pipe leading to the nozzle.
- Saturation Temperature ( $T_{sat}$ ) is obtained from standard water saturation tables, corresponding to the measured system pressure.
- Superheat Degree ( $\Delta T$ ) represents the temperature difference between the inlet fluid and its saturation temperature. Superheat is a critical factor in flash evaporation, as it determines the onset of phase change [39]:

$$\Delta T = T_i - T_{sat} \tag{10}$$

- Actual heat ( $\Delta T$ ) is calculated based on the difference between the inlet and the outlet temperatures of the liquid passing through the evaporator [40]:

$$\Delta T = T_i - T_o \tag{11}$$

The power provided to the system ( $Q_{evap}$ ) is calculated by multiplying the measured voltage and current supplied to the heater. The heat rejected by the condenser is determined using the following equation [41]:

$$Q_{cond} = \dot{m}_{w} (c p_{w} T_{w2} - T_{w1})$$
 (12)

where  $\dot{m}_w$  is the mass flow rate of the cooling water, and  $-T_{w1}$ ,  $T_{w2}$  are the inlet and outlet temperatures of the condenser cooling water.

Condenser thermal resistance (R<sub>cond</sub>) is the temperature difference across the condenser divided by the heat rejected:

$$R_{cond} = \frac{T_{sat} - T_{wc}}{Q_{cond}} \tag{13}$$

- Liquid mass flow rate  $(\dot{m}_l)$  refers to the volumetric flow rate of water entering the test section from the supply tank per unit time.
- Condensation mass flow rate ( $\dot{m}_{cond}$ ) represents the rate at which vapor is condensed and collected in the condensate tank. This factor is considered equal to the vapor mass flow rate from the nozzle under steady conditions.
- Flashing Efficiency (η)is the ratio of actual heat transferred during flashing to the maximum possible energy based on the degree of superheat, assumptions of constant Cp and non-equilibrium conditions.
- This factor is calculated using the following expression
   [42]:

$$\eta = \frac{\Delta T_{actual}}{\Delta T_{sup}} = \frac{T_i - T_o}{T_i - T_{sat}}$$
 (14)

These evaluation parameters provide insights into the thermal behavior, energy conversion efficiency, and overall performance of the wickless heat pipe system under flash evaporation conditions.

# **RESULTS AND DISCUSSION**

#### **Numerical Results**

Water evaporation under flashing conditions is investigated using numerical approaches. A parametric analysis is conducted to evaluate the sensitivity of the system to various inlet conditions. A selection of findings along the heat pipe with a jet nozzle is presented to illustrate the challenges of selecting appropriate intake settings. Measurements of inlet mass flow rate, inlet temperature, inlet pressure, and the inlet and outlet temperature and pressure of the condenser water jacket serve as an input to the CFD simulation. Numerical results are obtained for the velocity, temperature, and pressure profiles. The inlet temperature of water values is determined by five values, which are 373, 378, 383, 388, and 393 K. Figure 7(a-e) presents the numerical results of the temperature distribution along the vertical wickless heat pipe under rapid evaporation conditions. The figure shows the temperature gradually decreases, reaching its lowest value at the nozzle outlet. When the steam expanded at the throating section of the nozzle, the temperature decreases to below the saturation temperature. A decrease in energy absorbed by the droplets during evaporation is seen in the later profile, which displays a more realistic difference. The ambient temperature is reached. Because of the evaporation, the rise is first somewhat abrupt. Because droplets evaporate at a slow rate, there isn't an abrupt reduction in temperature; instead, it happens gradually over time. Figure 8(a-e) show the data simulation of the temperature distribution at evaporator section of straight heat pipe. Note that the figure represent the temperature distribution at different values of the inlet temperature (373K, 378K, 383K, 388K). As inlet temperature increases, the temperature gradient in the section increases, resulting in a wider distribution of high-temperature regions, as shown in the colors in the figure. The figure show that the highest temperature is near the heating area (bottom), and gradually decreases towards the top. As the inlet temperature increases, the heat distribution becomes more uniform in some regions, indicating improved heat transfer through the system. The red-colored regions increase as inlet temperature increases, indicating an increase in the total heat energy transferred through the system.

The velocity distribution in the vertical wickless heat pipe is quantitatively examined to investigate the vapor flow behavior under flash evaporation conditions. Velocity distribution for the operating condition of (373K, 378K, 383K, 388K, and 393K at 0.00138 kg/s) at the longitudinal section of the thermosyphon heat pipe (THP) is plotted in Figures 9 and 10(a-e). The larger number was computed under the

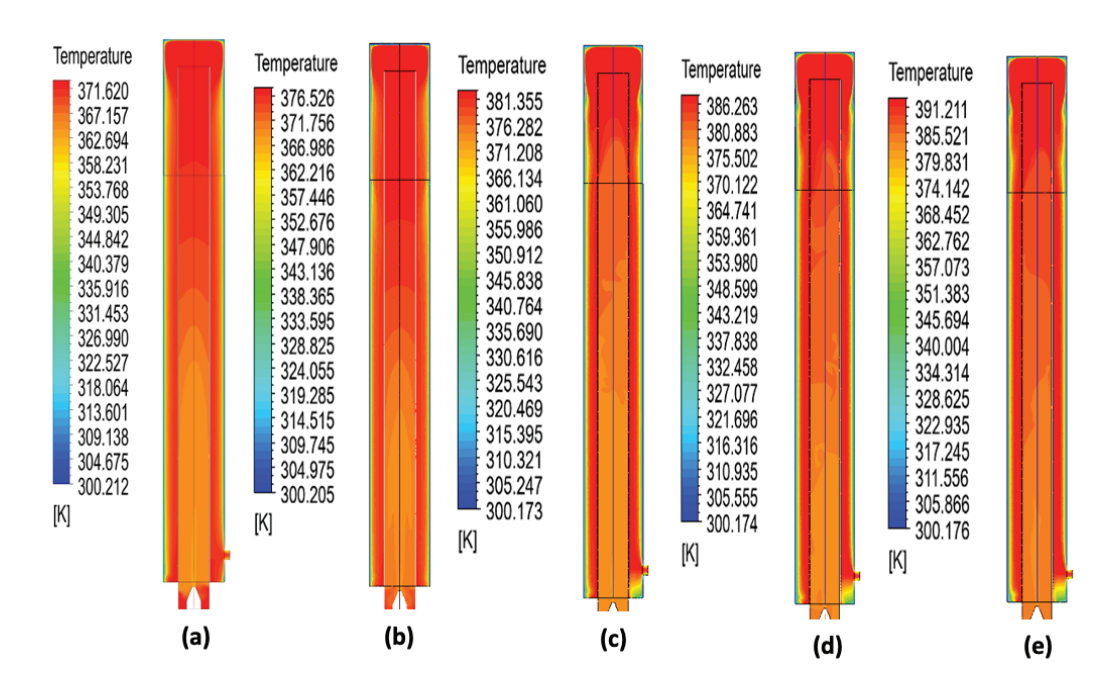


**Figure 7.** Numerical results of the temperature distribution for (a) 373K (b) 378 K (c) 383 K (d) 388 K (e) 393 K at inlet mass flow rate 0.00138kg/s.

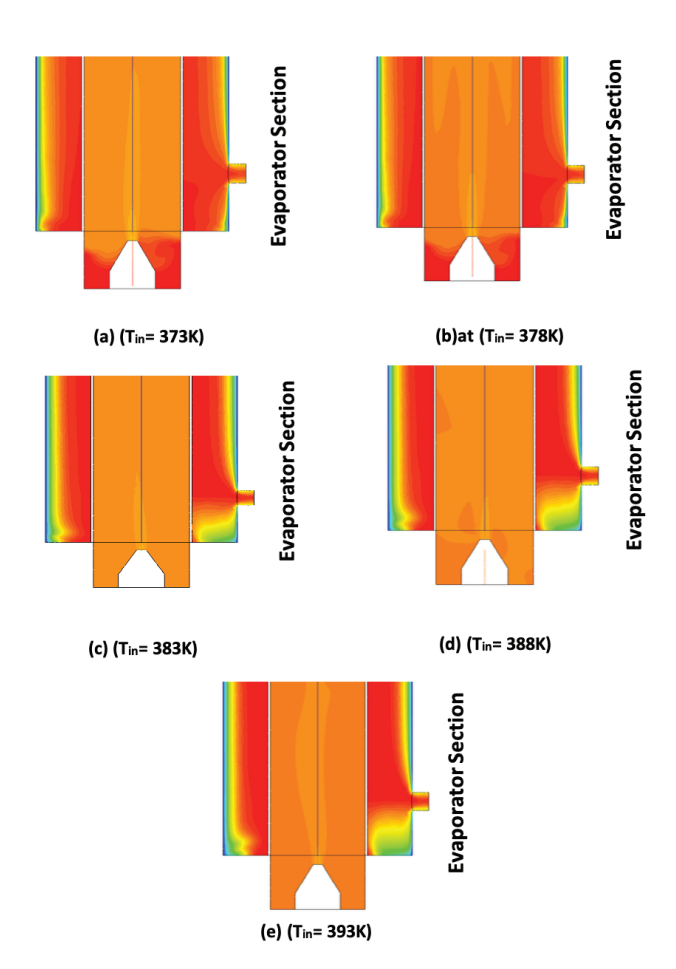


**Figure 8.** Numerical results of the temperature distribution of evaporator section for the SHP for (a) 373K (b) 378 K (c) 383 K (d) 388 K (e) 393 K at inlet mass flow rate 0.00138kg/s.

assumption that the nozzle exit velocity was determined by the maximal kinetic energy from the liquid cooling at flashing. On the other hand, the lower value was based on the idea that the storage pressure determines the velocity at which the spilled fluid emerges. Both velocity profiles exhibit a similar downward tendency. In this instance, the expected outcomes simply show that the measured value is near the input velocity, which was determined using the liquid's stagnation pressure. This assumption holds true when the volume of liquid inside the jet before flashing is modest compared to the surface area of the jet originating from the leak site. Flashing usually begins at the jet's corners for small leaks. In contrast, the jet's core spreads as a liquid, and this notion makes sense in these circumstances. The temperature profile is also significantly impacted by the beginning or intake velocity value. Therefore, to ensure the correct assumption is made when calculating velocity at the model intake, the inlet velocity can also be used to compare expected temperature profiles.

The two-phase flow patterns inside the SHP are characterized by a consistent behavior, where the steam predominantly flows upward near the inner surface of the evaporator section, while the condensate flows downward along the condenser side. This pattern, supported by three dimension numerical simulations of steam and liquid mass fractions, reflects a typical counter flow structure within the SHP. The steam and condensate streams remain confined near the wall. When these steams meet, the high-momentum stream influences the direction or momentum of the opposing flow. The flow patterns in the longitudinal and transverse sections of the straight heat

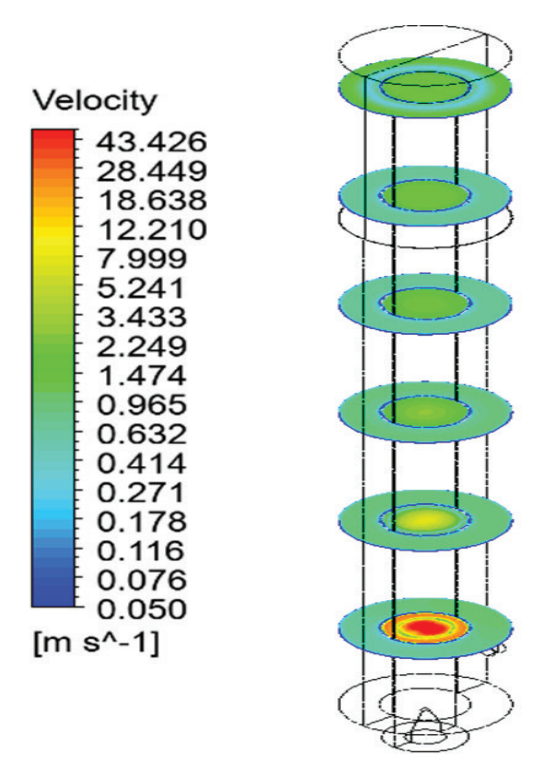


**Figure 9.** Numerical results of the velocity distribution for five inlet temperature.

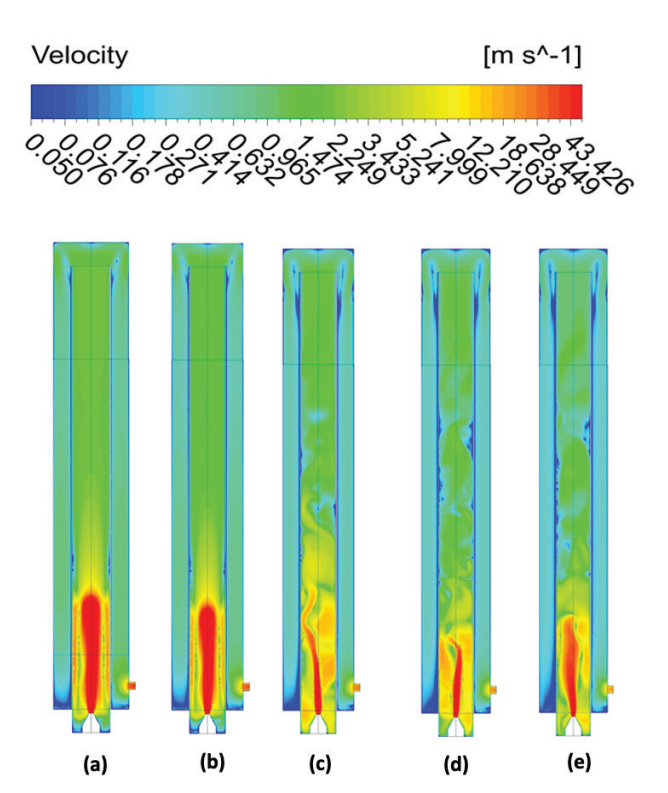


**Figure 10.** Numerical results of the velocity distribution for (a) 373K (b) 378 K (c) 383 K (d) 388 K (e) 393 K at inlet mass flow rate 0.00138kg/s.

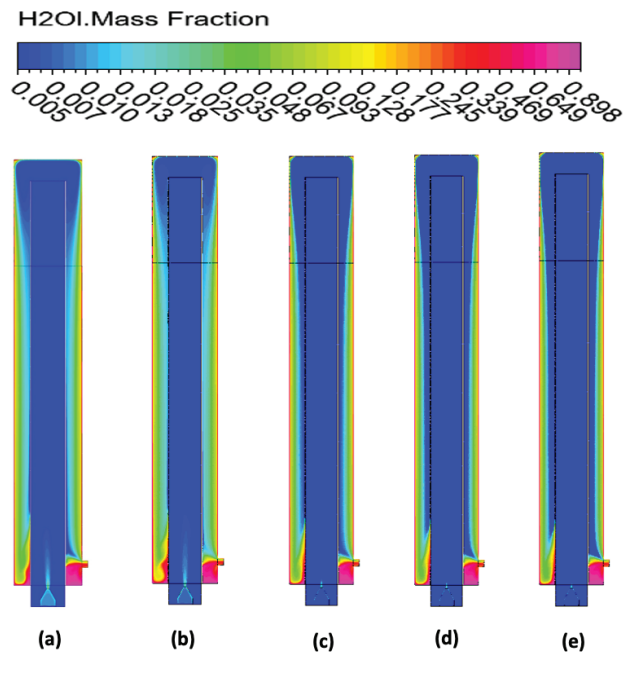


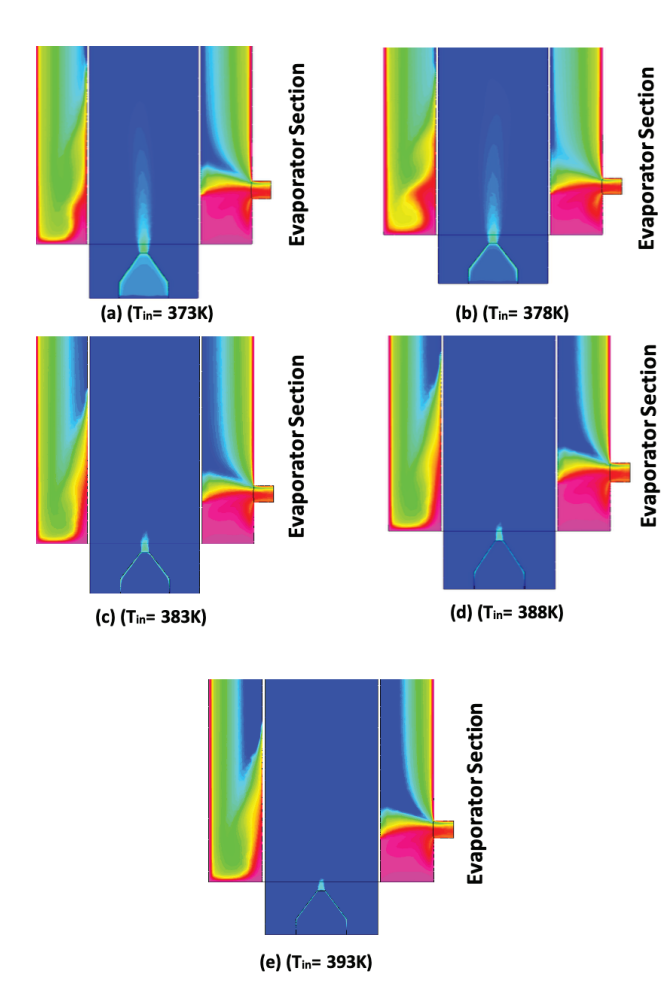
**Figure 11.** Numerical results of the liquid mass fraction distribution for (a) 373K (b) 378 K (c) 383 K (d) 388 K (e) 393 K at inlet mass flow rate 0.00138kg/s.

pipe are shown in Figure 11(a-e) and Figure 12(a-e) for operating conditions with inlet temperatures of 373K, 378K, 383K, 388K, and 393K, and an inlet liquid mass flow rate of 0.00138 kg/s as a sample. By comparing the mass fractions along the straight heat pipe with those in the jet nozzle, the model can be further evaluated. The generated steam continues to flow upward near the inner surface of the evaporator section of the wickless heat pipe. The condensate continues to flow downward near the inner surface of the condenser section of the straight heat pipe. The figures illustrate the distribution of water vapor concentration inside the tube. The highest vapor concentration is near the inlet area, indicated in red, and it gradually decreases towards the top, as indicated in blue. The blue areas indicate low water vapor concentration, suggesting that most of the vapor has condensed or separated from the mixture, which is consistent with thermal distillation mechanisms or heat exchange inside the thermal heat pipe. According to [1], the re-condensation of vapor is responsible for the mass fraction drop. In this investigation, the highest liquid mass fraction is 0.898.

# Comparison Between Numerical and Experimental Data

# Effect of the inlet temperature

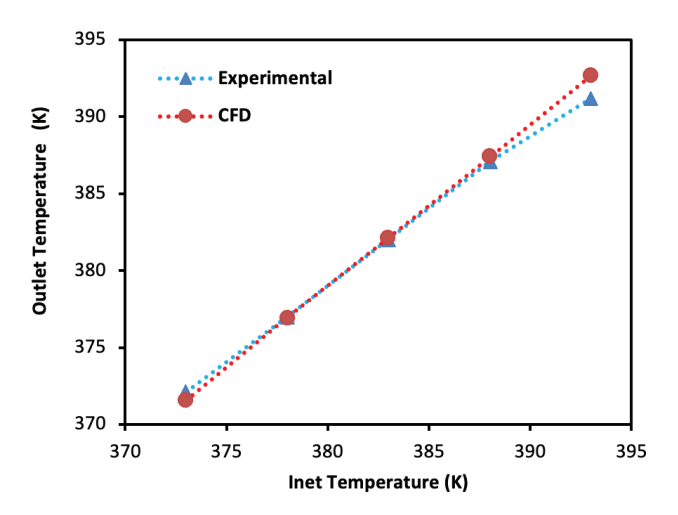
In this case, the study's numerical results and experimental measurements are compared. Figure 13 presents the comparison between the outlet vapor temperatures from the jet nozzle obtained numerically and experimentally at a mass flow rate of 0.00138 kg/s across five inlet temperature



**Figure 12.** Numerical results of the liquid mass fraction of the evaporator section for operating condition of (inlet tempture. (a)373K, (b)378K, (c)383K, (d)388K, (e) 393K.

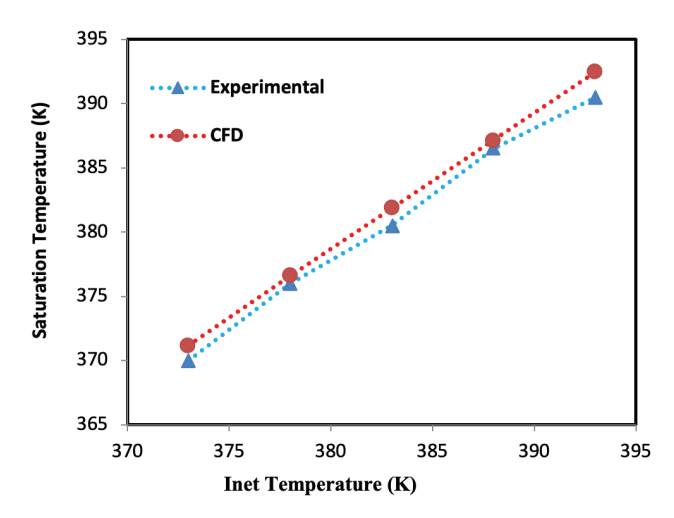
values. A strong correlation is observed between both datasets, showing that the outlet temperature increases with rising inlet water temperature. The maximum outlet temperature in the CFD results reaches 392.658 K. Minor discrepancies between the experimental and numerical results are noted, which can be attributed to practical factors such as heat losses to the surroundings, measurement uncertainties, and simplifications in the numerical model like assuming laminar flow and neglecting surface roughness or minor turbulence effects. Despite these, the overall agreement validates the accuracy and reliability of the numerical simulation.

Figure 14 presents a comparison between the experimental and numerical results for the saturation temperature under the same operating conditions as previously described. The figure demonstrates that the saturation temperature increases proportionally with the inlet temperature. This behavior is attributed to an enhanced boiling rate and a simultaneous increase in the wall temperature driven by the evaporation process.



**Figure 13.** Comparison between experimental and numerical results of the outlet temperature with five value of inlet temperature at 0.00138 kg/s liquid flow rate.

Since the wall temperature typically exceeds the saturation temperature by a certain margin, the heat transfer is sustained, and the saturation temperature correspondingly follows the wall temperature. Any change in the temperature gradient between the wall and the saturated fluid directly influences the boiling rate, thereby restoring thermal equilibrium within the system. The curve further illustrates the influence of flash evaporation on the saturation temperature of water along the test section. The saturation temperature was indirectly determined using the saturation pressure obtained from steam tables. Overall, the figure indicates good agreement between the experimental data and the numerical predictions, affirming the validity of the simulation approach.



**Figure 14.** Experimental and numerical results of the measured saturation temperature with five inlet temperature.

#### Condensation flow rate

The condensate flow rate was determined experimentally by conducting experimental tests. The amount of condensate flow rate determines the efficiency of the system, as the higher amount of condensate flow rate means that the flash evaporation effect is good. Figure 15 displays the experimental and numerical change of the condensate flow rate with inlet temperature for all liquid flow rates. The figure shows the condensate flow rate increases with increased liquid flow rate and increased inlet temperature. For the same amount of electricity, the evaporator's saturation pressure rises as the inlet temperature rises because the vapor space gets smaller. When the produced vapor comes into contact with a small area, it tends to rise in density; consequently, its saturation pressure (a process known as choking). The maximum flow rate of the condensate is 0.00134 kg/sec and 388k.

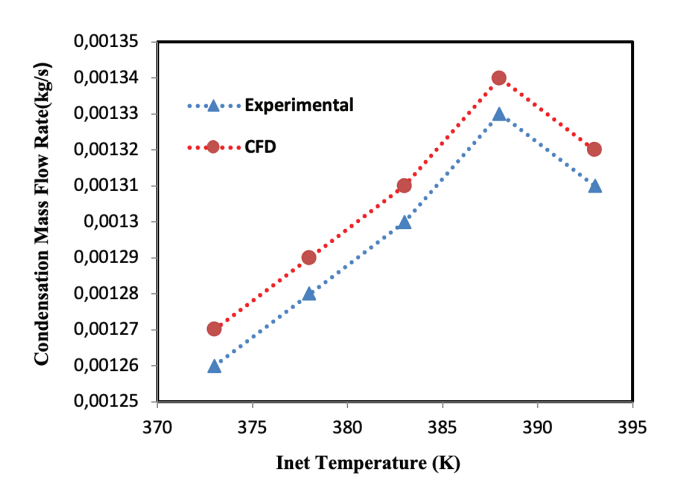


**Figure 15.** Experimental and numerical results of the measured condensation mass flow rate with the inlet temperature at 0.00138kg/s.

### Thermal resistance of the condenser

Thermal resistances of the condenser are found experimentally and numerically by equation (13). And the investigational changes of the observed condenser resistances with the inlet temperature for the inlet mass flow rate are portrayed in Figure 16. These figures manifest that as condenser thermal resistances increased when the evaporator inlet temperature increased. The minimum value of thermal resistance of the condenser is 0.036 (K/W) at 373 K for CFD results. The figure demonstrates that the experimental and numerical results correlate well. The numerical results of the condenser heat transfer coefficient are not available because it is considered a boundary condition for the simulation of the system. Figure 17 validation

between experimental results of the condenser heat transfer coefficient with inlet temperature. The figure shows the condenser coefficient decreases when the evaporator inlet temperature increases, and at an input temperature of 373 K and a liquid flow rate of 0.00138 kg/s, the condenser heat transfer coefficient reaches its maximum of 5059 W/m<sup>2</sup>.K.

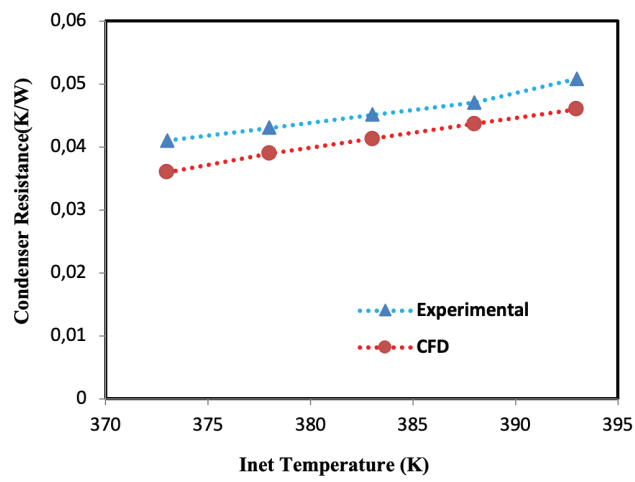


**Figure 16.** Experimental and numerical results of the measured condenser resistance with the five inlet temperature at 0.00138kg/s of liquid mass flow rate.

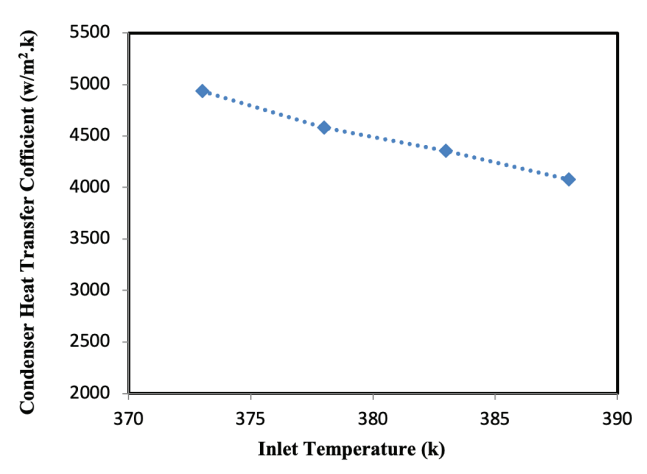


**Figure 17.** Experimental results of the measured condenser heat transfer coefficient with the inlet temperature at 0.00138kg/s liquid mass flow rate.

# Flash efficiency

The flash efficiency of the system was evaluated both experimentally and numerically using Equation (14). Figure 18 illustrates the relationship between flash efficiency and inlet temperature at a fixed inlet liquid mass

flow rate. The figure demonstrates a strong agreement between the experimental and numerical results, indicating the reliability of the simulation model. Flash efficiency is primarily influenced by the amount of vapor generated at the nozzle and is directly linked to the volume of condensate collected. A higher condensation rate reflects a more effective phase change, thereby enhancing the overall flash efficiency. The results reveal that flash efficiency increases with rising inlet temperature, reaching its maximum value of approximately 80% at 393 K. This indicates that higher inlet temperatures improve thermal performance and vapor generation, thus boosting the desalination effectiveness of the system.

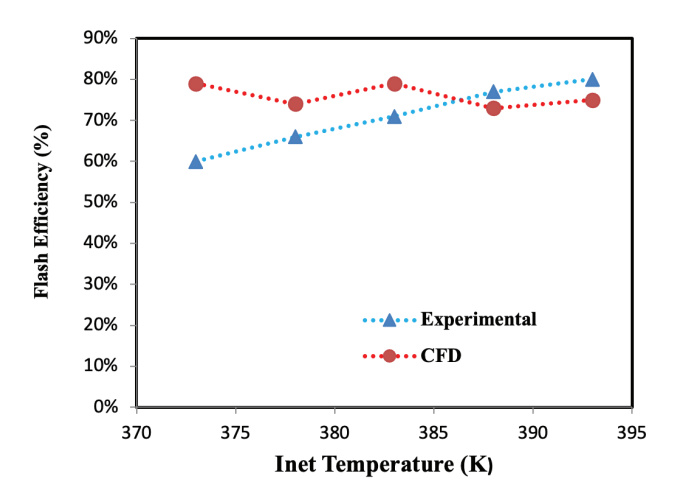


**Figure 18.** Experimental and numerical results of the measured flash efficiency with the five inlet temperature at 0.00138kg/s of liquid mass flow rate.

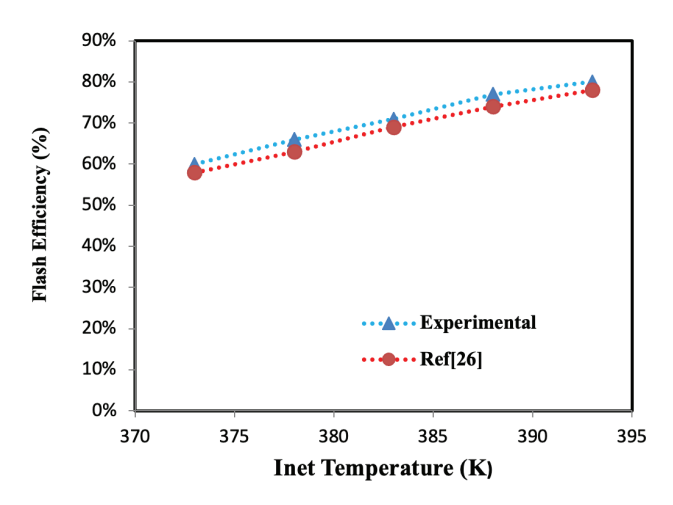


**Figure 19.** Comparison between the experimental and Ref [26] results of the measured flash efficiency with the five inlet temperature.

### Comparison with other work

A comparison with El-Fiqi et al. [26], who used superheated water jets to experimentally study flash evaporation under low-pressure settings, is done in order to validate the current findings. According to both experiments, flashing efficiency increases with superheat and inlet temperature. The current study, however, makes two significant improvements: it employs a 0.4 mm micro-nozzle to more accurately control flashing conditions and a closed wickless heat pipe (thermosyphon) in place of an open jet system. Furthermore, the work combines a non-homogeneous multiphase technique with 3D CFD modeling, enabling a thorough examination of phase transition and heat transport. The reliability and uniqueness of the suggested method for thermal desalination were confirmed by the measured flash efficiency in this work, which reached 80% at 393 K and was in good agreement with El-Fiqi's findings (Fig. 19).

# CONCLUSION

A comprehensive experimental and numerical investigation was conducted to evaluate the flash evaporation phenomenon in a wickless heat pipe system using water as the working fluid. The study particularly focused on flash evaporation induced by a superheated water jet injected through a 0.4 mm of diameter nozzle. The numerical simulation was carried out using the 3D ANSYS Fluent 22.2 software to model the evaporation and condensation processes.

Experiments were performed using inlet water temperatures ranging from 373 K to 393 K at a constant feed mass flow rate of 0.00138 kg/s. The analysis incorporated multiple performance indicators, including condensate flow rate, cooling water flow rate, flash efficiency, inlet temperature, and mass flow rate. The following key conclusions can be drawn:

- 1. Increasing the inlet water temperature leads to enhanced flash vapor generation, confirming the temperature's significant impact on the evaporation process.
- The condensate flow rate increases with both inlet temperature and liquid flow rate. At higher inlet temperatures, vapor formation intensifies, and when the vapor encounters a smaller volume, its density and saturation pressure increase (a phenomenon known as choking). The maximum condensate flow rate was observed at 388 K.
- 3. Flash efficiency improves with higher condensate flow rates and elevated inlet temperatures, reaching an optimal value of 80% at 393 K based on CFD results.
- 4. A strong agreement was observed between the numerical (CFD) simulations and the experimental results for the temperature profiles, validating the model's accuracy.

It is advised to investigate various nozzle geometries and materials in light of the findings in order to improve heat transfer performance and flash efficiency even more. Condensate return and vapor generation may also be enhanced by using multi-nozzle configurations and experimenting with different tilt angles. Future research can also

 $Cp_{w}$ 

concentrate on improving the CFD models for turbulent and transient situations and integrating the system with renewable heat sources.

# **NOMENCLATURE**

Specific heat of water (J/kg.°C) Evaporator, m<sup>2</sup>  $Cv_1$ Ε Energy (kJ) J/(kg.°C) Condenser heat transfer condenser (W/m2.°C)  $h_c$ Gravitational acceleration (m/sec<sup>2</sup>) g K Thermal Conductivity (W/m.°C) 1 liquid  $\dot{m}_w$ Mass flow rate of cooling water (kg/s) Р Pressure (kpa) Rejected power of the condenser(W) Q<sub>cond</sub>

Thermal resistance of the condenser (°C/W)

Specific heat of liquid water (J/kg.°C)

 $R_{cond}$ SE Energy source term (kJ) Density (Kg/m<sup>3</sup>)

ρ , T<sub>i</sub> Inlet temperature of the evaporator (°C)  $T_{o}$ Outlet temperature of the evaporator (°C)  $T_{w1}$ Inlet temperature cooling water (°C)  $T_{w2}$ Outlet temperature of cooling water (°C)

 $T_{sat}$ Saturation temperature (°C)

Time (Sec) t Vapor v Void Fraction  $\propto$ σ

Surface tension (N/m) Dynamic viscosity (N sec/m²) μ Specific volume (m³/kg) υ

V Velocity (m/sec)  $\vec{V}$ Velocity vector SHP Straight Heat Pipe Flash Efficiency (%)

# **ACKNOWLEDGMENTS**

The authors would like to express their sincere appreciation to Mustansiriyah University Baghdad, Iraq (www. uomustansiriyah.edu.iq) for their invaluable support in this research work.

# **AUTHORSHIP CONTRIBUTIONS**

Authors equally contributed to this work.

### **DATA AVAILABILITY STATEMENT**

The authors confirm that the data that supports the findings of this study are available within the article. Raw data that support the finding of this study are available from the corresponding author, upon reasonable request.

# **CONFLICT OF INTEREST**

The author declared no potential conflicts of interest with respect to the research, authorship, and/or publication of this article.

### **ETHICS**

There are no ethical issues with the publication of this manuscript.

# STATEMENT ON THE USE OF ARTIFICIAL INTELLIGENCE

Artificial intelligence was not used in the preparation of the article.

### REFERENCES

- Tay JH, Low SC, Jeyaseelan S. Vacuum desalination for water purification using waste heat. Desalination 1996;106:131–135. [CrossRef]
- Parfit M, Graves W. Water: the power, promise, and turmoil of North America's fresh water. Washington (DC): National Geographic Society; 1993.
- Khawaji AD, Kutubkhanah IK, Wie JM. Advances in seawater desalination technologies. Desalination 2008;221:47-69. [CrossRef]
- URS Australia. Introduction to desalination technologies in Australia. Report for Agriculture, Fisheries and Forestry-Australia; 2002.
- Raj MMA, Murugavel KK, Rajaseenivasan T, Srithar K. A review on flash evaporation desalination. Desalination Water Treat 2016;57:13462-13471.
- Aoki I. Water flash evaporation under low pressure conditions. Prev Heat Mass Transf 1995;6:518.
- Saury D, Harmand S, Siroux M. Flash evaporation from a water pool: influence of the liquid height and of the depressurization rate. Int J Therm Sci 2005;44:953-965. [CrossRef]
- Jouhara H, Reay D, McGlen R, Kew P, McDonough J. [8] Heat pipes: theory, design and applications. Oxford: Butterworth-Heinemann; 2023.
- Payakaruk T, Terdtoon P, Ritthidech S. Correlations [9] to predict heat transfer characteristics of an inclined closed two-phase thermosyphon at normal operating conditions. Appl Therm Eng 2000;20:781-790. [CrossRef]
- [10] Park YJ, Kang HK, Kim CJ. Heat transfer characteristics of a two-phase closed thermosyphon to the fill charge ratio. Int J Heat Mass Transf 2002;45:4655-4661. [CrossRef]
- Vasiliev LL. Heat pipes in modern heat exchangers. [11] Appl Therm Eng 2005;25:1–19. [CrossRef]
- Liu ZH, Li YY. A new frontier of nanofluid research [12] - application of nanofluids in heat pipes. Int J Heat Mass Transf 2012;55:6786-6797. [CrossRef]
- Mameli M, Mangini D, Vanoli GFT, Araneo L, [13] Filippeschi S, Marengo M. Advanced multi-evaporator loop thermosyphon. Energy 2016;112:562-573. [CrossRef]

- [14] Alammar AA, Al-Dadah RK, Mahmoud SM. Numerical investigation of effect of fill ratio and inclination angle on a thermosiphon heat pipe thermal performance. Appl Therm Eng 2016;108:1055–1065. [CrossRef]
- [15] Schreiber M, Wits WW, te Riele GJ. Numerical and experimental investigation of a counter-current two-phase thermosyphon with cascading pools. Appl Therm Eng 2016;99:133–146. [CrossRef]
- [16] Naresh Y, Balaji C. Experimental investigations of heat transfer from an internally finned two-phase closed thermosyphon. Appl Therm Eng 2017;112:1658–1666. [CrossRef]
- [17] Naruka DS, Dwivedi R, Singh PK. Experimental inquisition of heat pipe: performance evaluation for different fluids. Exp Heat Transf 2020;33:668–682. [CrossRef]
- [18] Górecki G, Łęcki M, Gutkowski AN, Andrzejewski D, Warwas B, Kowalczyk M, et al. Experimental and numerical study of heat pipe heat exchanger with individually finned heat pipes. Energies 2021;14:5317. [CrossRef]
- [19] Abdulrasool AA, Temimy AAB. Thermal performance enhancement of a vertical thermosyphon heat pipe by flow control of the two phases. J Eng Sustain Dev 2021;25:1. [CrossRef]
- [20] Al-Sa'di SE, Al-Tabbakh AA, Abdulrasool AA. Experimental comparative study of straight and loop wickless heat pipes with rectangular evaporator and water cooled condenser. Heat Mass Transf 2022;58:695–705. [CrossRef]
- [21] Höhne T. CFD simulation of a heat pipe using the homogeneous model. Int J Thermofluids 2022;15:100163. [CrossRef]
- [22] Al Jubori AM, Jawad QA. Computational evaluation of thermal behavior of a wickless heat pipe under various conditions. Case Stud Therm Eng 2020;22:100767. [CrossRef]
- [23] Al Jubori AM, Jawad QA. Computational evaluation of thermal behavior of a wickless heat pipe under various conditions. Case Stud Therm Eng 2020;22:100767. [CrossRef]
- [24] Wang X, Liu H, Xue Y, Wu N, Gan W, Zhu Y. Experimental and CFD investigation on the thermal performance of two-phase closed thermosyphons: effect of corrugated evaporator. Appl Therm Eng 2024;257:124494. [CrossRef]
- [25] Adnan SE, Kassim MS, Alderoubi N, Aljibori HSS, Ibrahim SY, Mahmood RA, et al. Numerical study of a wickless heat pipe for cooling of electronic component. Int J Heat Technol 2024;42:1660–1670. [CrossRef]
- [26] El-Fiqi AK, Ali NH, El-Dessouky HT, Fath HS, El-Hefni MA. Flash evaporation in a superheated water liquid jet. Desalination 2007;206:311–321.
- [27] Izzat AW, Addaiy RM. Flash evaporation enhancement by electrolysis of saturated water flowing upwards in vertical pipe. J Eng 2010;16:5620–5632.

  [CrossRef]

- [28] Łapka P, Seredyński M, Grzebielec A, Szelagowski A, Śmiechowicz M, Gromadzki E. Numerical investigation of the effect of the shape of the nozzle on the flash boiling phenomenon. E3S Web Conf 2019;128:07005. [CrossRef]
- [29] Fathinia F, Al-Abdeli YM, Khiadani M. Evaporation rates and temperature distributions in fine droplet flash evaporation sprays. Int J Therm Sci 2019;145:106037. [CrossRef]
- [30] John S, Lange CF. A limited evaporation model for flashing applications. Int J Heat Mass Transf 2024;225:125351. [CrossRef]
- [31] Cai B, Shen J, Deng Q, Zhang Y. Experimental investigation on thermal characteristics of spray flash evaporation under high temperature and high pressure. Ann Nucl Energy 2021;163:108513.
- [32] Ji C, Liu Z, Lü M. Numerical investigation of the flash evaporation process inside a nozzle with two S-shaped internal vanes in a waste heat power generation system. Shandong Sci 2021;34:89–96.
- [33] Cai B, Shen J, Deng Q, Zhang Y. Modeling of spray flash evaporation under high temperature and high pressure based on droplet analysis. At Energy Sci Technol 2021;55:1935–1942.
- [34] ANSYS Inc. ANSYS FLUENT Theory Guide. Canonsburg (PA): ANSYS Inc.; 2018.
- [35] Vallée C, Höhne T, Prasser HM, Sühnel T. Experimental investigation and CFD simulation of horizontal stratified two-phase flow phenomena. Nucl Eng Des 2008;238:637–646. [CrossRef]
- [36] Fluent Inc. Fluent 14.5 User Guide. Lebanon (NH): Fluent Inc.; 2002.
- [37] FEA Tips. How to verify mesh quality in ANSYS Workbench. Available at: https://featips.com/2021/05/07/how-to-verify-mesh-quality-in-ansys-workbench/#google\_vignette Accessed on Nov 03, 2025.
- [38] Ali Z, Tucker PG, Shahpar S. Optimal mesh topology generation for CFD. Comput Methods Appl Mech Eng 2017;317:431–457. [CrossRef]
- [39] Sadeq AH, Shehab SN. An experimental investigation of turbulent forced convection into a horizontal finned eccentric annulus. J Mech Eng Res Dev 2020;43:113–125.
- [40] Muthunayagam AE, Ramamurthi K, Paden JR. Low temperature flash vaporization for desalination. Desalination 2005;180:25–32. [CrossRef]
- [41] Chen YJ, Wang PY, Liu ZH, Li YY. Heat transfer characteristics of a new type of copper wire-bonded flat heat pipe using nanofluids. Int J Heat Mass Transf 2013;67:548–559. [CrossRef]
- [42] Raj MMA, Murugavel KK, Rajaseenivasan T, Srithar K. A review on flash evaporation desalination. Desalination Water Treat 2016;57:13462–13471.

  [CrossRef]